J. Fluid Mech. (1995), *vol.* 294, *pp.* 181–207

Air entrapment by a falling water mass

By HASAN N. OĞUZ[1] ANDREA PROSPERETTI[1] AND ALI R. KOLAINI[2]

[1] Department of Mechanical Engineering, The Johns Hopkins University, Baltimore, MD 21218, USA

[2] National Center for Physical Acoustics, University of Mississippi, Oxford, MS 38677, USA

(Received 13 September 1994 and in revised form 12 January 1995)

The impact of a nearly cylindrical water mass on a water surface is studied both experimentally and theoretically. The experiments consist of the rapid release of water from the bottom of a cylindrical container suspended above a large water tank and of the recording of the free-surface shape of the resulting crater with a high-speed camera. A bubble with a diameter of about twice that of the initial cylinder remains entrapped at the bottom of the crater when the aspect ratio and the energy of the falling water mass are sufficiently large. Many of the salient features of the phenomenon are explained on the basis of simple physical arguments. Boundary-integral potential-flow simulations of the process are also described. These numerical results are in fair to good agreement with the observations.

1. Introduction

The dull sound accompanying the falling of a mass of water onto a water surface is very commonly experienced. It was speculated by Minnaert (1933) and proven by Franz (1959) that this sound is caused by the oscillations of air bubbles, and it is the twin aspects of noise generation and air entrainment that motivate more than a passing interest in this process. On the acoustic side, it has been shown in recent years that air entrainment is the dominant contributor to oceanic ambient noise over a broad frequency range extending from a few tens of Hz to hundreds of kHz (Prosperetti 1988; Medwin & Beaky 1989; Medwin & Daniel 1990; Farmer & Ding 1992; Lamarre & Melville 1994; Loewen & Melville 1994; Hollett 1994; Ding & Farmer 1994; Kolaini & Crum 1994).

Depending on conditions (e.g. near the coast, or at very high sea states) an important fraction of the low-frequency component of this noise is directly due to waves breaking in the plunging mode and to the impact of splashes. In industry, air entrainment is actively pursued in certain water aeration systems and gas–liquid chemical reactors. Ship bow waves falling back onto the water surface also entrain bubbles that, in addition to causing noise, can be transported to the propeller region and act as nuclei for undesirable cavitation events. The process can also be encountered during the initial transient of an otherwise steady or quasi-steady flow such as a jet falling onto a liquid. Even when no air is entrained in the steady state, some bubbles may be generated when the jet first contacts the liquid surface.

Several recent papers have been devoted to the related process of air entrainment by impacting drops (Pumphrey & Crum 1988, 1990; Pumphrey, Crum & Bjørnø 1989; Pumphrey & Elmore 1990; Longuet-Higgins 1990; Oğuz & Prosperetti 1989, 1990, 1991; Prosperetti & Oğuz 1993; Chahine *et al.* 1991; Stroud & Marston 1993). In the

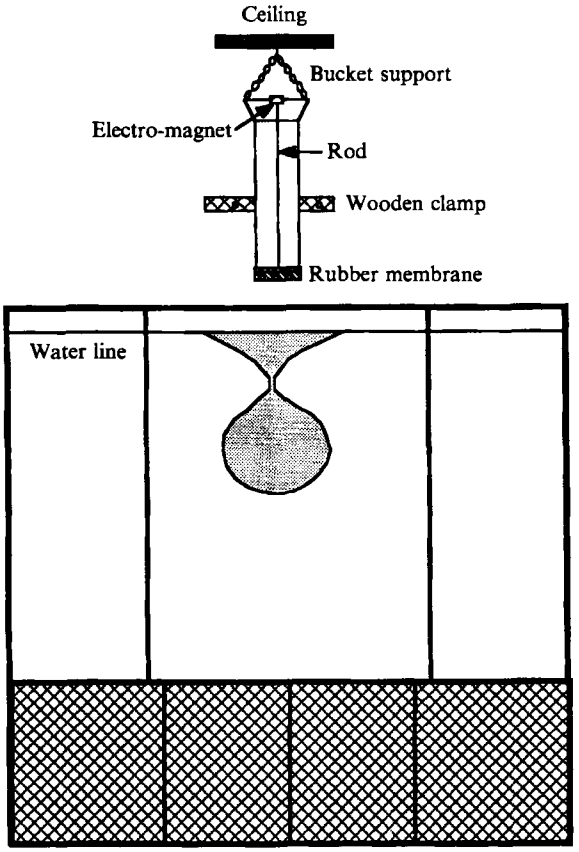

FIGURE 1. Sketch of the experimental set-up with the Plexiglas tank. The tank dimensions are 2.1 m × 2.1 m × 1.8 m (width, length, depth).

present theoretical and experimental study we consider instead liquid masses – 'splashes' – so large that the motion is dominated by gravity and inertia while surface tension is negligible. The experiment simply consists of releasing cylindrical volumes of water from less than 0.1 to nearly 11 litres onto the quiescent surface of a water tank. As a consequence of the impact the free surface forms a crater that grows, penetrates downward, and finally pinches off entraining a large gas bubble. It is at this point that a strong pulse of low-frequency sound is emitted. While the quantitative aspects of this study only refer to the normal impact of cylindrical water masses, it may be expected that this general sequence of events applies quite generally to sufficiently energetic impacts.

The acoustic aspects of this work have already been reported (Kolaini *et al.* 1993). Here, we focus on the fluid mechanics. After a brief review of the experiment, we present an analysis of the process based on simple physical considerations. The paper concludes with the description of the results of numerical simulations by an inviscid boundary-integral method.

The suggestion for this experiment was originally made by Longuet-Higgins (1989) to simulate in the laboratory the acoustic emission from a breaking wave.

2. Experimental set-up

A detailed description of the experimental set-up can be found in Kolaini *et al.* (1993). Here we present a brief summary.

The experiments were carried out in a laboratory tank with dimensions of 2.1 m × 2.1 m × 1.8 m (width, length, and height) filled with tap water and maintained at ambient temperature (23 °C). Cylindrical containers suspended 40–355 mm above the tank and restrained from lateral movement were used to release the water (figure 1). The containers had diameters 30–183 mm and were filled with tap water up to heights 50–450 mm. A tightly stretched thin rubber sheet secured by a rubber band closed the container's bottom. To initiate the experiment, thin sharpened rods suspended a few inches above the membrane were released and ruptured it. This caused the water to fall onto the tank's still-water surface, producing a cavity the evolution of which was recorded with a Kodak Ekta-Pro high-speed video camera operating at a rate of 1000 frames per second and fitted with a Nikon 28-mm lens. The camera was directed perpendicular to the cavity axis as viewed through the Plexiglas wall. The sound produced in the course of the process was also recorded synchronously with the video for later processing. A Photec IV rotating-prism motion picture camera operating at 500 frames per second was also used with a wide variety of lenses and multipliers to capture images both of the free falling jet and of the evolution of the entrained cavity.

The characteristic dimensions of the crater and of the entrained bubble were measured from the video or film images. In a few cases, the entrained air was captured by means of a device described in Kolaini *et al.* (1993) and its volume measured directly. In general, good agreement between the bubble volume obtained from the images and that measured directly was found.

3. Experimental results

Figure 2 shows frames from a high-speed movie sequence of the rupture of the rubber membrane and the release of the liquid slug. Here the radius of the container is 54 mm, the depth of the water in the container is 0.45 m, and the suspension height 0.15 m from the tank water surface. The time elapsed between the first and the last frame shown is 262 ms. The tip of the rods that have just pierced the membrane are visible in the third frame. Full rupture of the membrane is completed in less than 1 ms. The liquid falls as a cylinder only approximately, with several nearly axisymmetric surface disturbances of various wavelengths clearly visible from frame (vi) onward. The relatively long-wavelength wave near the bottom is probably due to the relaxing of the initial shape of the liquid mass. The shorter waves above originate as the liquid leaves the tube but are also affected by the impact with the underlying undisturbed liquid. The lower surface of the falling water appears very disturbed. The last frame shows that the upper surface of the water in the container does not remain flat even though horizontal movement of the container is restrained. The nature of this apparent instability is not immediately clear. In particular, the original photos clearly show that the container is vertical, so that it does not appear plausible that it be due to a misalignment with gravity.

In spite of the presence of surface waves, the falling liquid mass maintains essentially its initial shape during the impact, a fact that may at first sight be surprising in view of the stagnation point that must exist somewhere near its base. This feature can be explained by noting that, since the aspect ratio is rather large and the pressure at the

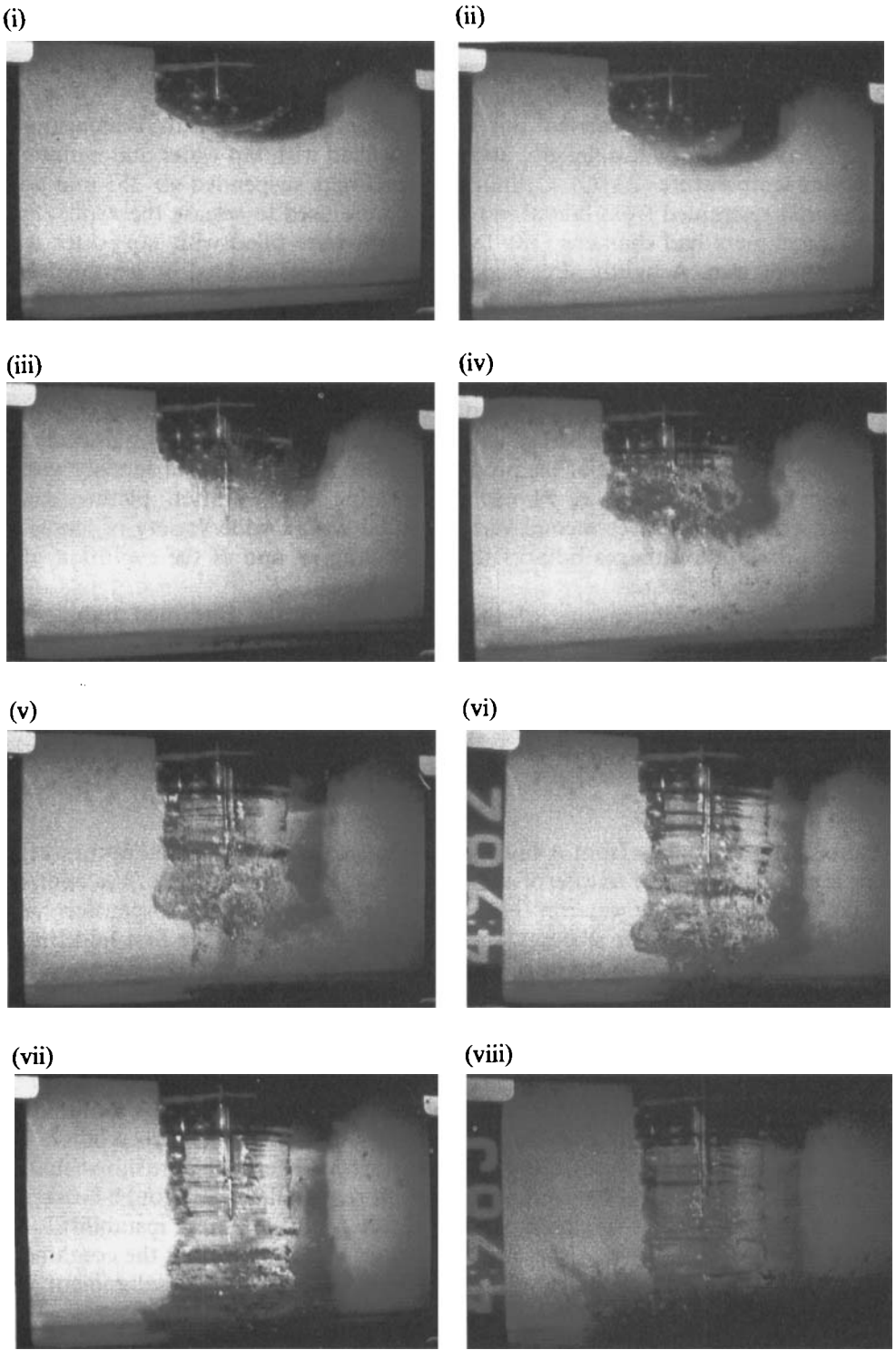

FIGURE 2(i)–(viii). For caption see facing page.

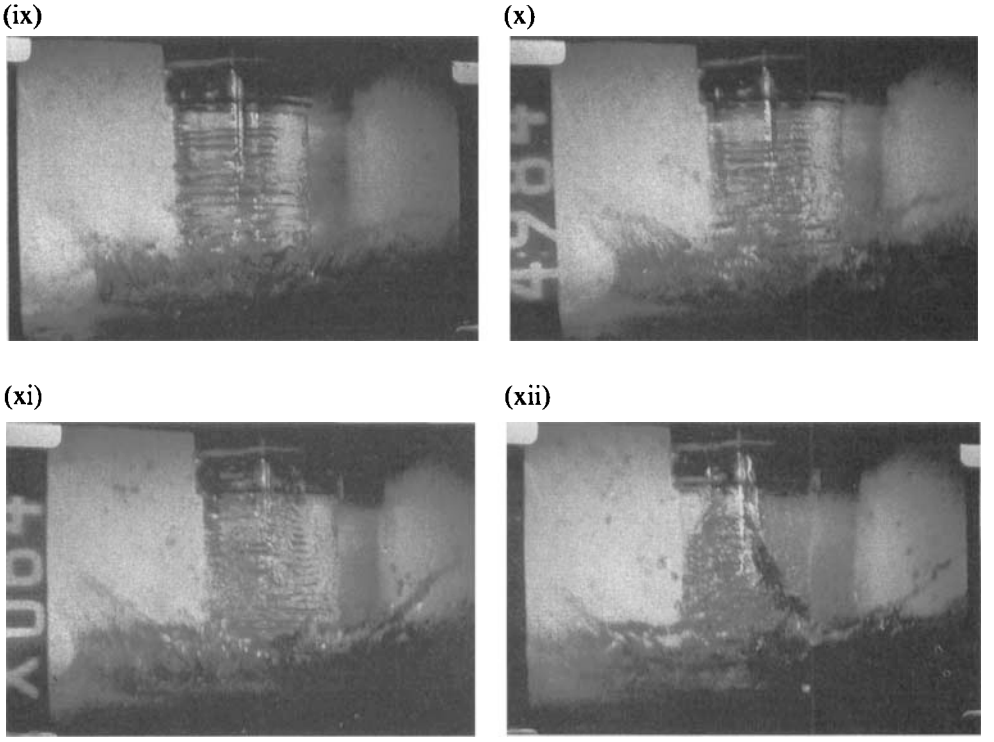

FIGURE 2. High-speed move sequence (500 f.p.s.) of the rupture of the rubber membrane and the release and fall of the liquid slug. Container radius $r = 54$ mm, water depth $h = 0.45$ m, suspension height $d = 0.15$ m. Times elapsed after the first frame are 2, 30, 80, 120, 140, 160, 180, 200, 220, 242 and 262 ms.

surface constant (atmospheric), axial pressure gradients in the falling liquid are not easily generated.

Figure 3 shows a view in the water of another event obtained in the same experimental conditions. A bubble is entrapped by the pinching off of the large air crater that is generated by the impact. The pinch-off occurs because of a convergence of the liquid on the axis of symmetry. Since the convergence is only approximate, some air remains entrapped along the axis with the appearance of a 'stem' connecting the large cavity to the tank free surface. The sudden impact of the radial closure creates a high-pressure region that deflects the liquid partly upward and partly downward. The upward jet is the familiar one that one sees when an object (e.g. a stone) is thrown into water. The downward-directed jet hits the bottom of the bubble much in the same way as the original jet hit the undisturbed water surface. A 'third-generation' jet formed by the same mechanism is sometimes observed. This 'cascading' effect has the consequence of entraining air at greater depths than one would otherwise expect. Although not clear from this particular sequence, the cavity surface is quite smooth throughout the growth period, but roughens considerably with short-scale capillary waves completely covering it at the moment of pinch-off. Figure 4 is a closeup view taken in the same experimental conditions. The liquid jet inside the bubble is visible in the first frame. The sequence shown in this figure is typical of impacts with sufficient initial energy. When the distance of free fall is lower or the water mass smaller the crater is less pronounced and a large number of small bubbles (possibly together with a bigger bubble at the centre)

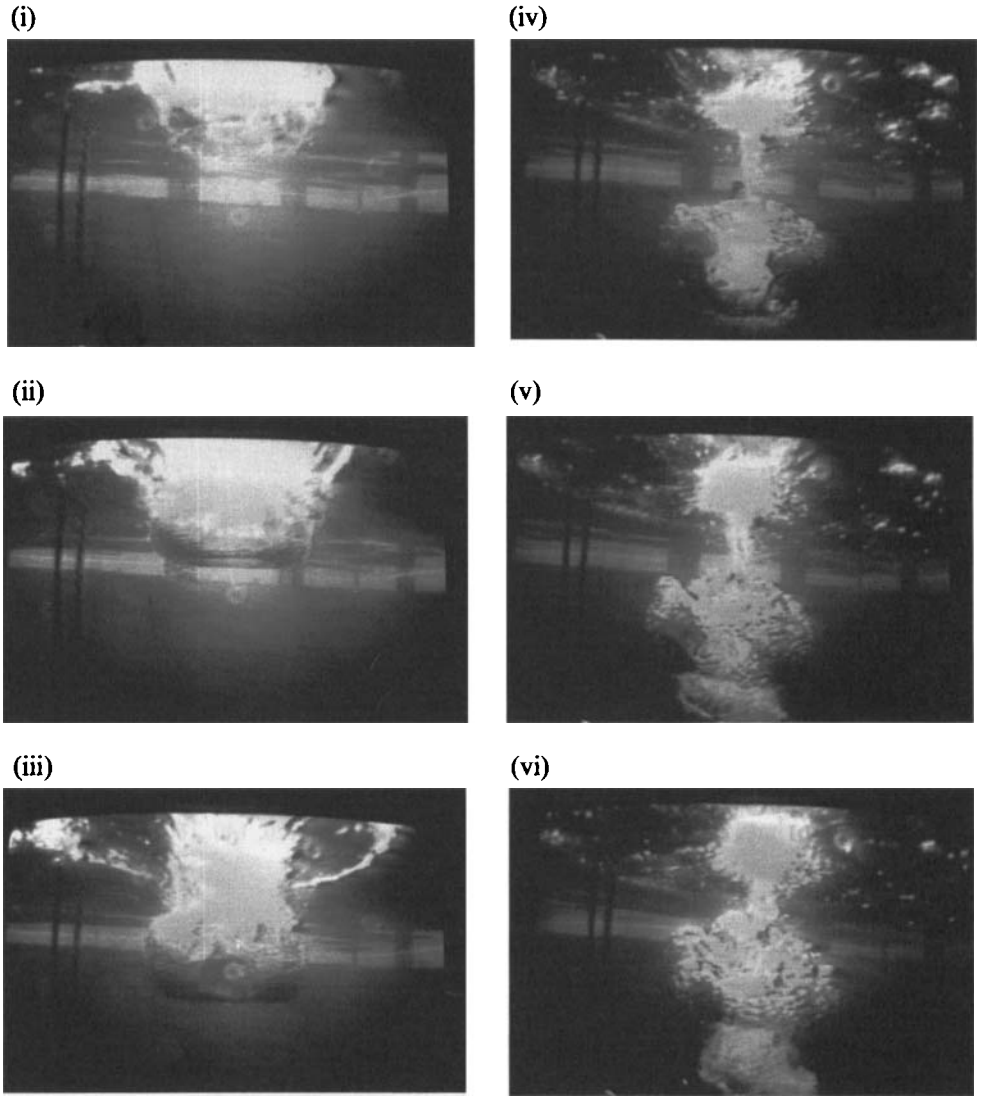

FIGURE 3. The air entrapment process in the same experimental conditions as in figure 2 as recorded by an underwater video camera at normal speed. The last three frames show the downward penetration of the secondary jet caused by pinch-off into the lower cavity surface. Another bubble will be formed by the impact of this secondary jet. The frames shown are approximately 150, 200, 255, 340, 400 and 600 ms after release of the liquid. These images were taken in the course of an experiment in Puget Sound with sea water.

is entrained. An example of this type is given below in figure 19. Until then, we shall only deal with energetic impacts.

This air-entrainment process is in some respects similar to the mechanics of bubble entrainment by impacting millimetre-size drops (see e.g. Prosperetti & Oğuz 1993). This remark is rather interesting in view of the large differences in the magnitude of surface-tension forces that give a Weber number of the order of 10^2 for the drop cases, and of the order of 10^3 here. Some comments on this point will be found at the end of §4.

The general shape of the air boundary at the moment of bubble detachment as

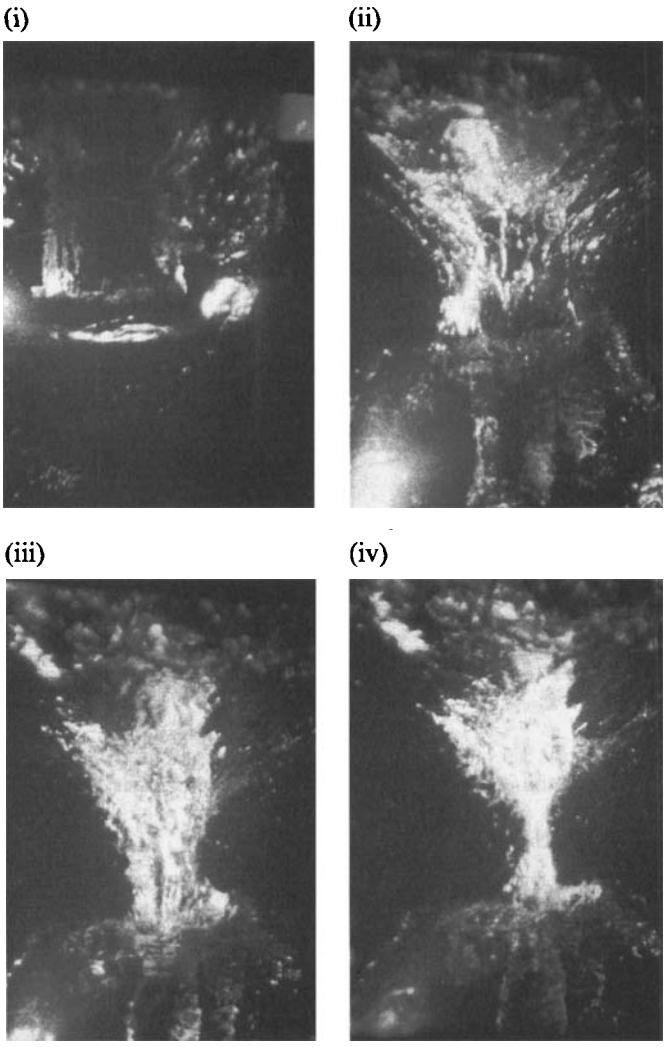

FIGURE 4. Another example of bubble entrapment from closer range for the same experimental conditions of figure 3. The entering water column is visible through the cavity surface in the first frame. Filming rate is 500 f.p.s. The times are 230, 290, 295 and 297 ms after release of the liquid.

revealed by the visualization studies is shown in figure 5, which also defines some nomenclature. The basic geometric features on which we focus in the following are: the depth H of the lowest point on the bubble surface; the depth D of the pinch-off point below the undisturbed free surface; the bubble equivalent spherical radius R_B.

Experimentally the independent variables are (figure 5) the radius r of the cylindrical container, the depth h of the water in the container, and the suspension height d of the bottom of the container above the undisturbed water surface. These parameters were varied in the range $50 \leqslant h \leqslant 450$ mm, $15 \leqslant r \leqslant 91.5$ mm, $40 \leqslant d \leqslant 355$ mm. The corresponding impact velocities on the basis of free fall neglecting air resistance range from 0.88 to 2.64 m s^{-1}.

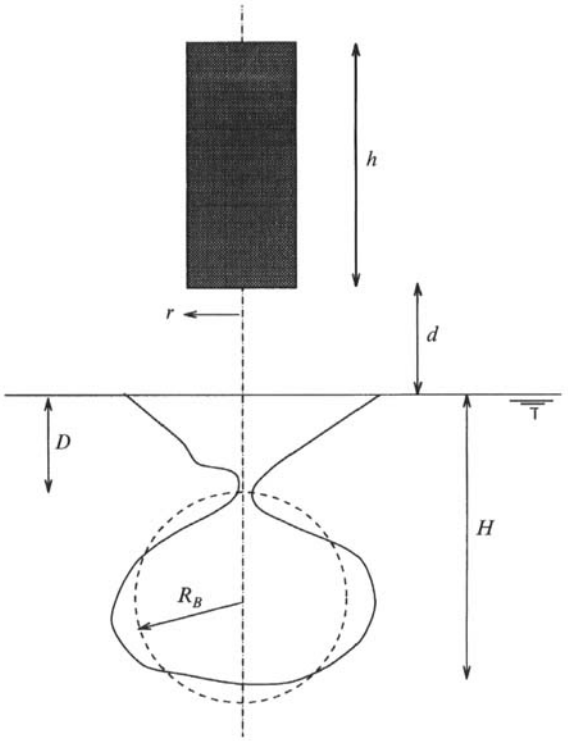

FIGURE 5. Definition of the geometric parameters of the problem. Note in particular that R_B is the *equivalent* spherical radius of the cavity.

4. Physical considerations

Before being released, the mass M of water has the potential energy $Mg(d+\frac{1}{2}h)$ where g is the acceleration due to gravity. If this initial potential energy is converted to kinetic energy, $\frac{1}{2}MU^2$, one deduces the characteristic velocity

$$U = [2g(d+\tfrac{1}{2}h)]^{1/2}. \tag{1}$$

The Froude, Weber, and Reynolds numbers defined in terms of r and U are

$$Fr = \frac{h}{r}\left(1+2\frac{d}{h}\right), \tag{2}$$

$$We = \frac{\rho g}{\sigma} rh\left(1+2\frac{d}{h}\right), \quad Re = \frac{r}{\nu}\left[g\left(1+2\frac{d}{h}\right)\right]^{1/2}, \tag{3}$$

where σ, ρ, and ν denote surface tension, density, and kinematic viscosity. In all the cases investigated experimentally the Reynolds and Weber numbers are large enough that viscous and surface-tension effects are negligible. (As will be seen later in §6 this statement must be qualified. It is however sufficiently accurate for the present purposes.) Hence, aside from g, each experiment can be considered as fully characterized by the three lengths r, h, and d or, in dimensionless form, by the two parameters h/r and Fr. A map of this parameter space showing the experimental points is shown in figure 6, where the straight lines are lines of constant d/h. It also follows that any measured quantities l or V with dimensions of length or velocity may be written as

$$\frac{l}{r} = F_1\left(\frac{h}{r}, Fr\right), \quad \frac{V}{U} = F_2\left(\frac{h}{r}, Fr\right). \tag{4}$$

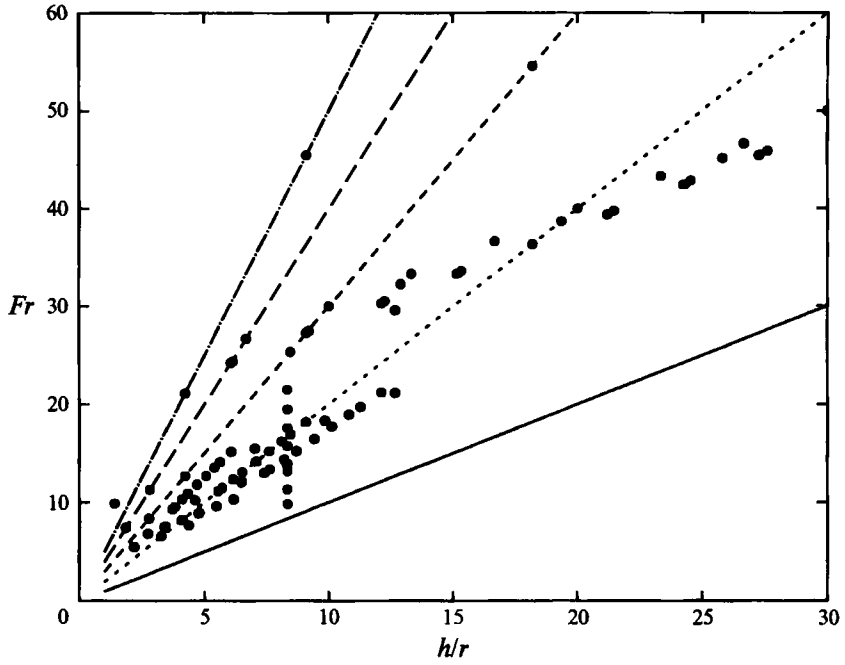

FIGURE 6. Parameter space with the experimental points. The d/h = const. lines are, in ascending order, for $d/h = 0$ (solid line), 0.5, 1, 1.5 and 2.

Physical arguments are needed to simplify further these general expressions.

Let us first consider the speed at which the cavity surface progresses downward after the initial impact (figure 3). To the extent that gravity effects can be neglected in the evolution of the free surface (which presupposes a high Froude number, or high-energy impacts), this velocity V is readily shown to equal half the impact velocity (Birkhoff & Zarantonello 1957, p. 16; Oğuz, Lezzi & Prosperetti 1992). Indeed, in a frame of reference where the bottom of the crater is stationary, an observer sees a liquid column, or jet (see e.g. figure 14), impinging with a velocity $U-V$ while the liquid ahead of the jet is moving toward the jet with a velocity V. This must also be the velocity along the outer surface of the cavity far away from the impact point, since the flow velocity there must equal the undisturbed incoming velocity V. However, since the pressure in the cavity is uniform, Bernoulli's theorem requires that the magnitude of the velocity along the cavity surface be constant, i.e. $V = U-V$, from which $V = \frac{1}{2}U$. This prediction agrees very well with data on hyper-velocity impacts seen in collapsing bubbles and underwater explosion bubbles. Its accuracy in the present situation can be judged from figure 7 where the dotted lines are from measurements and the dashed line from the calculation to be described in §6. It is seen that both experiment and numerical modelling agree very well with this estimate in spite of the unsteady nature of the actual flow, gravity, and the presence of boundaries.

For sufficiently energetic impacts we can also estimate the width of the cylindrical air cavity surrounding the jet (see e.g. figure 14). For this purpose we note that, in a reference frame in which the bottom of the crater is stationary (figure 8), there is an analogy with the flow established by a source (the incoming liquid) immersed in a uniform flow (the pool liquid in the moving frame). The situation is sketched in figure 8 in which part (*a*) shows the jet flow and part (*b*) the flow produced by a source in a

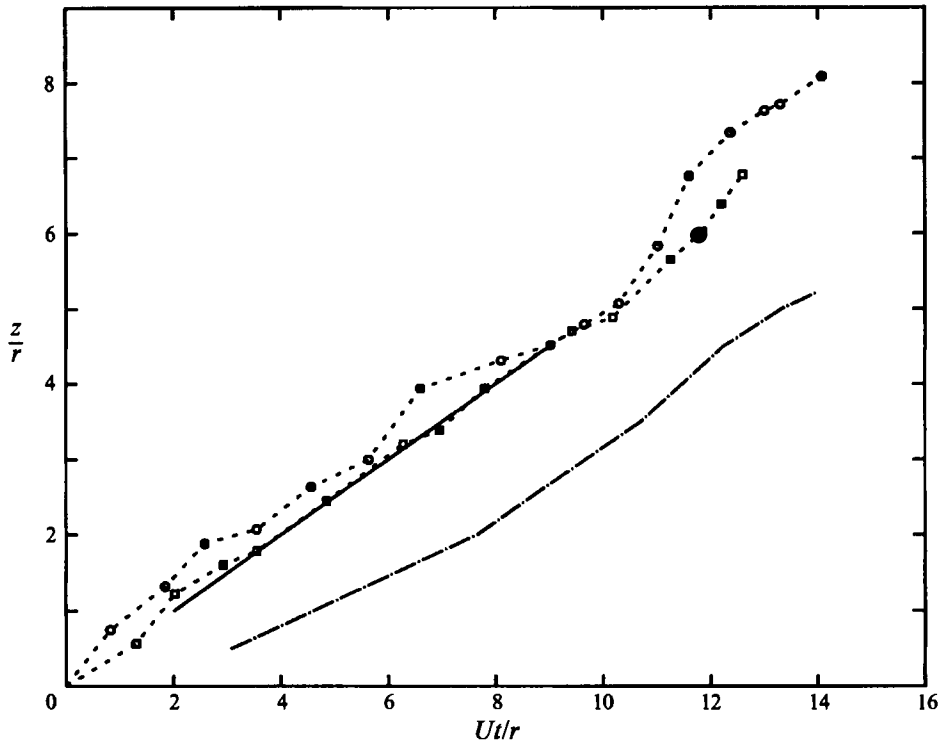

FIGURE 7. Depth of the cavity front versus time according to experiment (dotted lines) and the calculations of §6 (dash-and-dot line). The solid line is the simple estimate from a front velocity equal to $\frac{1}{2}U$. The experimental points are for $r = 5.4$ cm, $h = 30$ cm, $d = 15$ cm (squares) and $r = 5.4$ cm, $h = 40$, $d = 15$ cm (circles).

uniform stream with velocity $V = \frac{1}{2}U$. This is precisely the situation in the well-known theory of Rankine bodies in potential flow. The velocity potential for such a flow is

$$\phi = Q/4\pi r + Vr\cos\theta, \tag{5}$$

where Q is the source strength, V the free-stream velocity, and r, θ spherical coordinates centred at the source. For this flow the locus of all points with vanishing axial velocity is

$$V = (Q/4\pi r^2)\cos\theta. \tag{6}$$

To determine a value of Q giving rise to a flow that approximates the jet entry problem, we require that the locus (6) contain a point with radial velocity $\frac{1}{2}U$, so that

$$\tfrac{1}{2}U = -(Q/4\pi r^2)\sin\theta. \tag{7}$$

Physically, we have required that the lowest point of the cavity surface (along all of which, from Bernoulli's theorem, the velocity equals $\frac{1}{2}U$) match in position and velocity the corresponding point of the source flow. The simultaneous equations (6) and (7) imply that $\tan\theta = -1$ and that

$$Q = 4\pi r^2 V. \tag{8}$$

The radius S of the Rankine body corresponding to this source flow is

$$S = (Q/\pi V)^{1/2} = 2r. \tag{9}$$

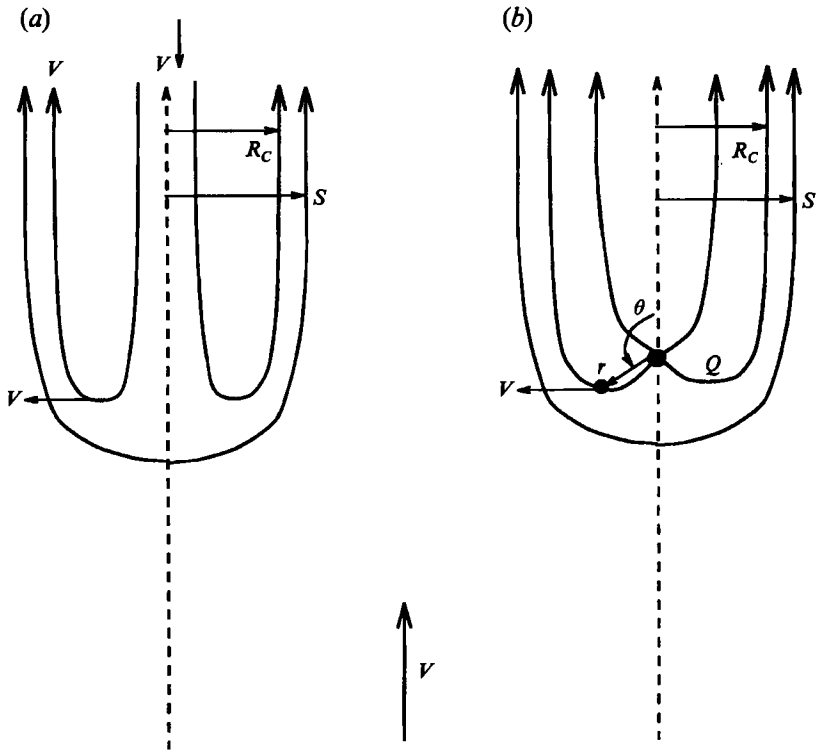

FIGURE 8. (*a*) Sketch of the water entry process in a frame of reference in which the cavity front is stationary. (*b*) Comparison with a Rankine half-body flow. Here $V = \frac{1}{2}U$.

The jet liquid is deflected at the stagnation point and 'coats' the inner side of the Rankine body flow, far from the turning point, at the same speed $\frac{1}{2}U$, as follows from the Bernoulli equation. Conservation of mass then requires that $\frac{1}{2}U\pi(S^2-R_C^2) = \frac{1}{2}U\pi r^2$ from which

$$R_C \approx (S^2-r^2)^{1/2} = \sqrt{3}r. \tag{10}$$

Experimental data of R_C/r versus h/r for several experiments are shown in figure 9. Here R_C is measured directly from the films at the moment of pinch-off. In a few cases the width of the crater was monitored during its growth and it was found to remain constant and equal to its value at pinch-off as would be expected on the basis of the previous considerations. In figure 9 the radius of each circle showing a data point is proportional to the value of the Froude number. More precisely, *Fr* equal 500 times the circle radius measured on the vertical scale of the figure. The smallest circle corresponds to $Fr = 9.81$, and the largest one to $Fr = 45.5$. It can be seen that, for sufficiently energetic impacts (large h/r and *Fr*), which are the only ones for which the preceding argument is applicable, R_C/r is indeed approximately constant, although the value 2 rather than $\sqrt{3}$ seems a better fit to the data. Similar results are found in the numerical calculations described in §6. For shorter jets the crater is closer to hemispherical rather than cylindrical as in the case of the drop impacts studied in Oğuz & Prosperetti (1991) and the quantity R_C is not well defined and is difficult to measure. This explains the scatter in the data in this region.

Let us now return to the maximum depth of the crater. Here we must consider several cases, depending on the jet length, as shown in figure 10.

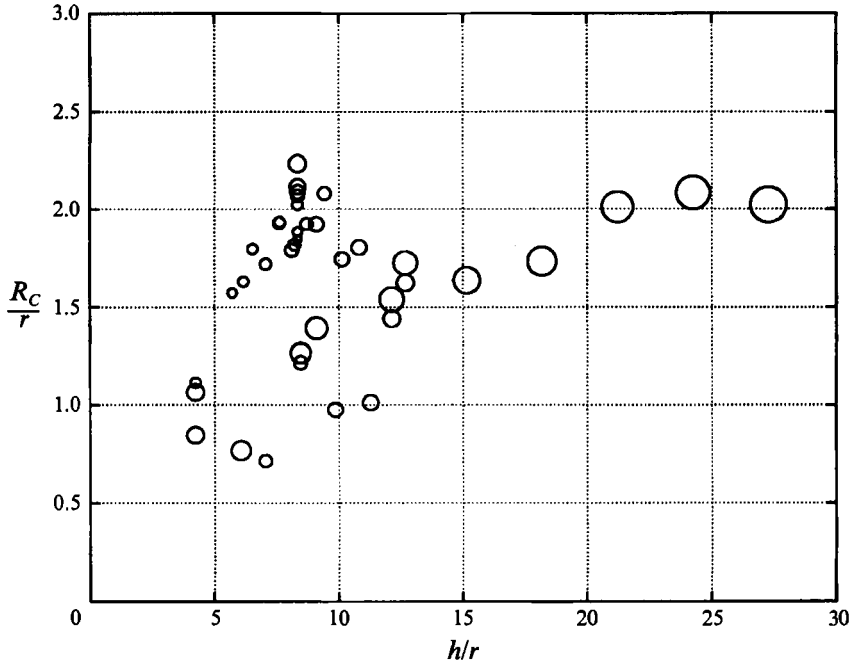

FIGURE 9. Measured data for the dimensionless cavity width R_c/r versus h/r (circles). The Froude number equals the radius of the circles measured on the vertical scale multiplied by 500. The smallest circles are for $Fr = 9.81$ and the largest ones for $Fr = 45.45$.

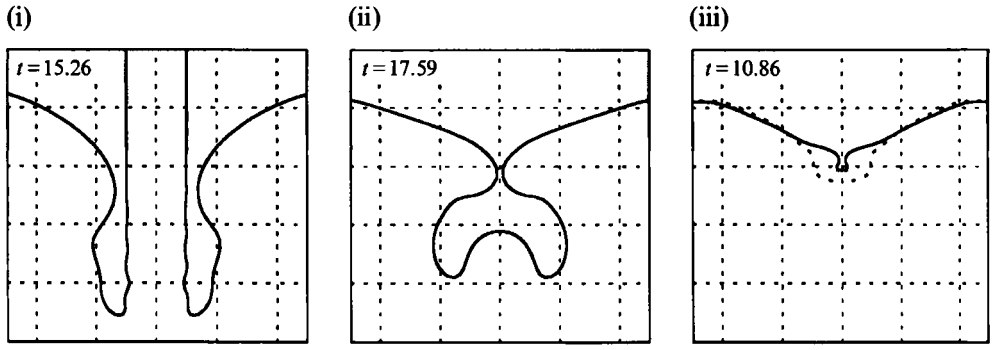

FIGURE 10. Numerical examples (according to the numerical computations of §6) of the three regimes for bubble entrapment: (i) $h/r = \infty$, $d/r = 33.98$; (ii) $h/r = 13.28$, $d/r = 2.78$, and (iii) $h/r = 3.70$, $d/r = 2.78$. The dashed line in (iii) indicates the cavity shape at the moment of deepest penetration.

(i) For long jets, the jet 'tail' is above the pinch-off point and the cavity closes against the jet surface (figure 10i). It will be seen from figure 13 below that very few of the present experiments fall in this range. A computational example is shown in figure 1 of Oğuz *et al.* (1992) and in figure 10(i). Here $h/r = \infty$, $d/r = 33.98$ and $(2gd)^{1/2}t/r = 15.3$.

(ii) As the jet gets shorter, at the moment the cavity closes the jet 'tail' is still above the cavity bottom, but below the pinch-off point (figure 10ii, for $h/r = 13.28$, $d/r = 2.78$) at $Ut/r = 17.60$;

(iii) For even shorter jets, the jet has completely disappeared below the cavity bottom by the time pinch-off occurs and, actually, the bottom liquid has already

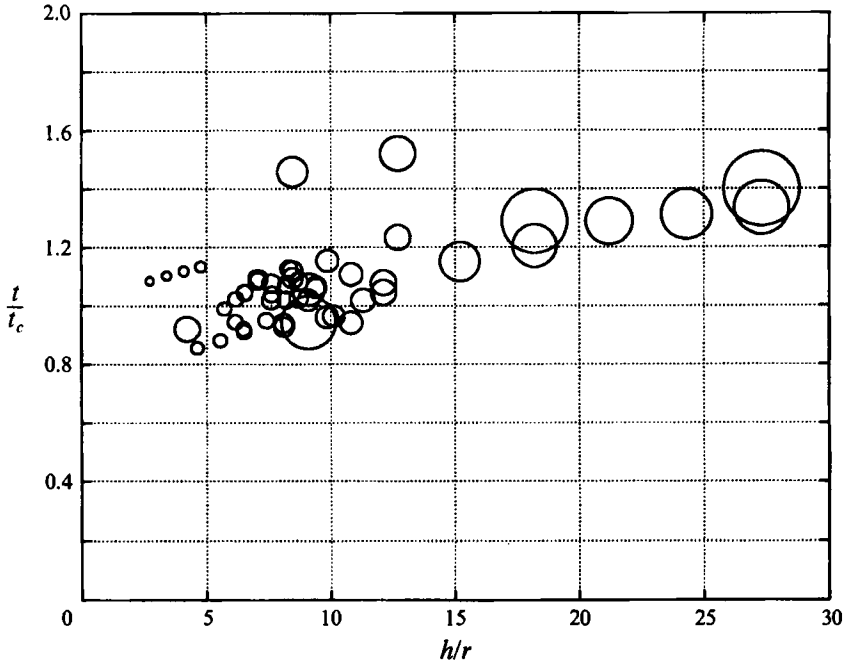

FIGURE 11. Observed closure time of the cavity divided by the estimate (14) for different h/r and Fr. Scaled as described for figure 9, the smallest circles are for $Fr = 6.8$ and the largest ones for $Fr = 63.66$.

started to move upward (figure 10iii, for $h/r = 3.70$, $d/r = 2.78$, $Ut/r = 10.86$; the dashed line here is the crater shape at the moment of maximum depth where $Ut/r = 10.38$).

To estimate the time of cavity closing in regimes (i) and (ii) we use the following simple conceptual model. Consider a horizontal layer of liquid at a depth z below the undisturbed free surface. At a time of the order of $z/(\frac{1}{2}U)$ after the initial contact of the impacting liquid, this layer is reached by the advancing crater that creates a hole of radius $R_C \approx 2r$. After its formation the hole starts collapsing radially inward and we assume that this collapse process for the layer at z proceeds independently from that at other depths. Since the collapse itself is driven by the hydrostatic pressure difference between the liquid and the cavity, it may be assumed to occur with a characteristic velocity $(gz)^{1/2}$ so that it will be completed in a time of the order of $R_C/(gz)^{1/2}$. The hole at depth z will have completely collapsed therefore after a time

$$\frac{2z}{U} + \beta \frac{R_C}{(gz)^{1/2}} \tag{11}$$

from the initial impact, where the constant β is expected to be of order 1. The moment t_c at which the air cavity first closes, or pinches off, can be found by looking for the minimum of this function which occurs for $z = D$, given by

$$\frac{D}{r} = \left(\tfrac{1}{4}\beta \frac{R_C}{r}\right)^{2/3} Fr^{1/3}, \tag{12}$$

and is

$$\left(\frac{g}{r}\right)^{1/2} t_c = \frac{3}{2}\left(2\beta \frac{R_C}{r}\right)^{2/3} Fr^{-1/6}. \tag{13}$$

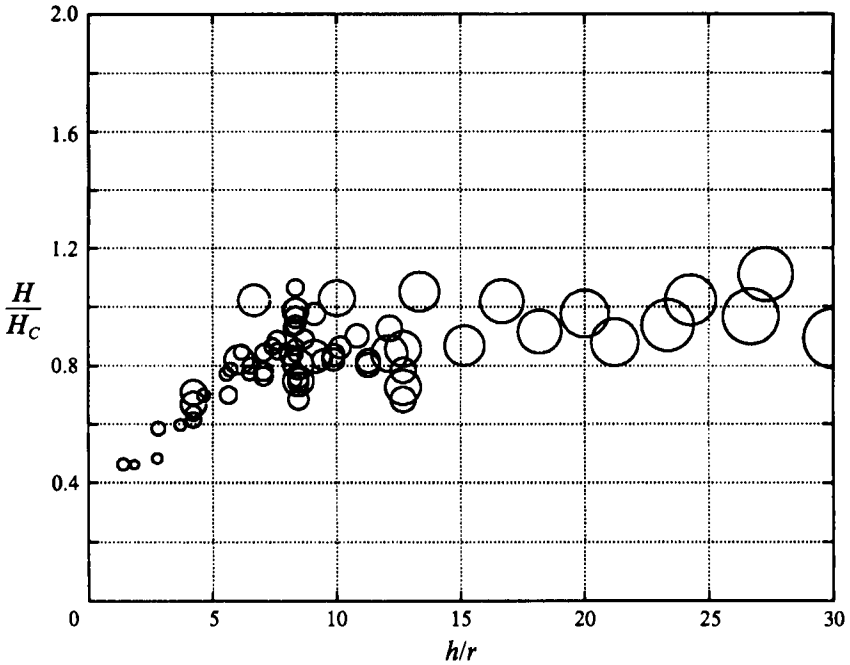

FIGURE 12. Measured crater depth divided by (16) for different h/r and Fr. The smallest circles are for $Fr = 7.41$ and the largest ones for $Fr = 50$.

In deriving these results R_C/r has been considered a constant. In regime (i), since part of the cavity's mouth is occupied by the jet, one might expect a somewhat shorter time. This effect could be accounted for by a somewhat smaller value of β, although the dependence on this quantity is not strong and it might be difficult to determine experimentally. The results obtained upon taking $R_C/r = 2$ and $\beta = 2$ in (13), i.e.

$$(g/r)^{1/2} t_c = 6Fr^{-1/6}, \tag{14}$$

are tested against the data in figure 11. This particular value of β has been chosen in order to have simple round numbers rather on the basis of a formal procedure that would have little justification in view of the scatter of the data. In spite of some scatter, the prediction (14) is supported by the data.

The depth H_C of the crater formed in regimes (i) and (ii) (i.e. for sufficiently long jets) can now be estimated as $\frac{1}{2}Ut_c$ and is therefore

$$\frac{H_C}{r} = \frac{3}{4}\left(2\beta \frac{R_C}{r}\right)^{2/3} Fr^{1/3}. \tag{15}$$

It may be noted that $H_C = 3D$. Figure 12 shows the observed cavity depth divided by (15) with $R_C/r = \beta = 2$ as before, i.e.

$$H_C/r = 3Fr^{1/3}. \tag{16}$$

Here the radius of each circle is proportional to Fr as explained before in connection with figure 9. The scaling suggested by (16) seems to be supported for h/r greater than about 6–8. The closing depth D cannot be measured reliably from the movies as the flow velocities near pinch-off are too large for a proper resolution.

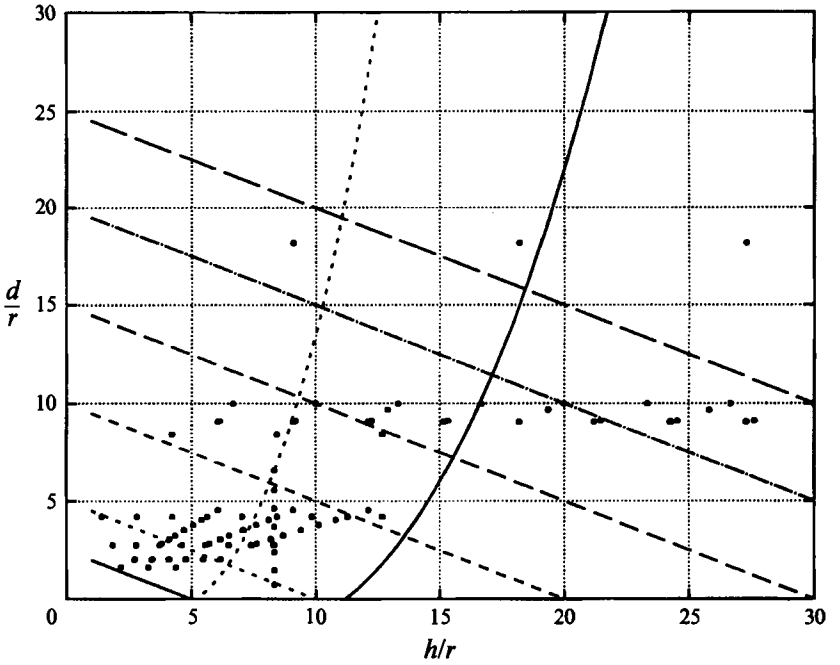

FIGURE 13. The solid curve corresponds to the transition between regimes (i) and (ii) of figure 10, the dashed curve to the transition between (ii) and (iii). The points indicate the experimental tests conducted in this study. The nearly parallel lines are constant-*Fr* lines corresponding to, in ascending order, $Fr = 5, 10, 20, 30, 40, 50$.

The jet length $h_{2\text{-}3}$ corresponding to the transition between regimes (ii) and (iii) must be given by $h_{2\text{-}3} + H_C = Ut_c$, as the tail of the jet travels the distance in the left-hand side with a velocity U. This simply gives

$$h_{2\text{-}3} = H_C = 3rFr^{1/3}. \tag{17}$$

By a similar argument, the jet length corresponding to the transition between regimes (i) and (ii) must be given by $h_{1\text{-}2} + D = Ut_c$ or

$$h_{1\text{-}2} = \tfrac{5}{3}H_C = 5rFr^{1/3}. \tag{18}$$

Upon using the definition (2) of the Froude number, we find

$$\frac{d}{r} = \frac{1}{2}\left[\left(\frac{1}{N_{ij}^3}\frac{h_{i\text{-}j}}{r}\right)^3 - \frac{h_{i\text{-}j}}{r}\right], \tag{19}$$

where $N_{12} = 5$ and $N_{23} = 3$. These lines are shown in figure 13 together with points marking the cases investigated experimentally. The family of other nearly parallel lines in this figure corresponds to fixed values of *Fr*. Unfortunately the visual resolution was too poor to determine to which regime each particular experimental point belonged and therefore it is not possible to check the prediction (19) against the data.

We show in figure 14 the cavity evolution, as computed numerically by the method described below, corresponding to a borderline case between regimes 1 and 2. Here $h_{1\text{-}2}/r = 40/3$ and $d/r = 25/9$. It is seen in the next-to-last frame that the cavity is just about to close onto the jet tail, so that the prediction is fairly accurate.

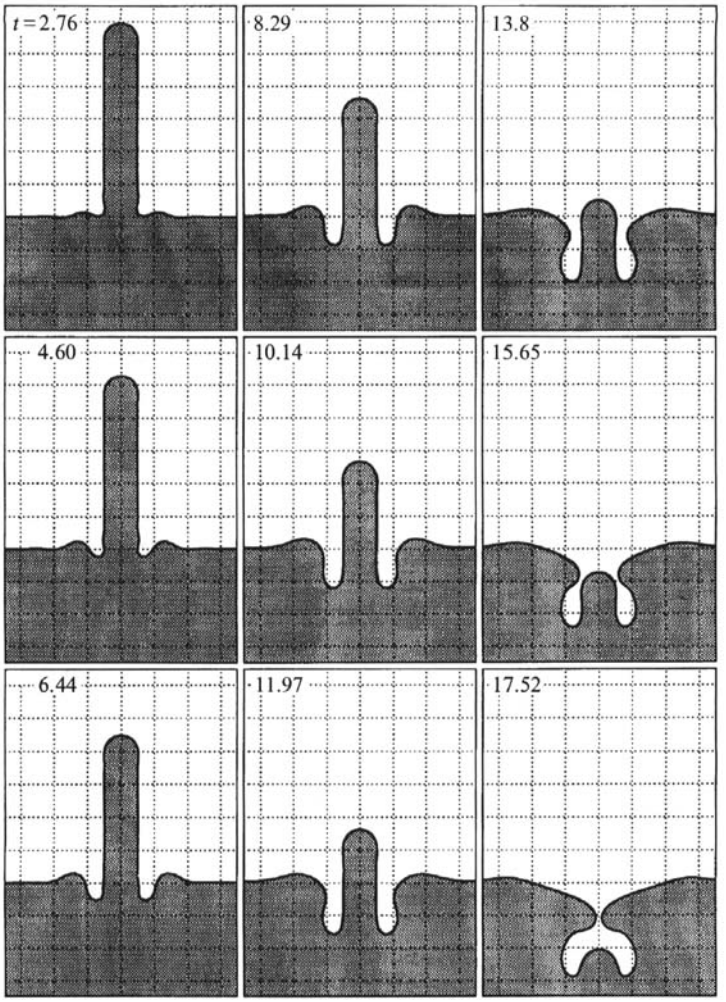

FIGURE 14. Computed free-surface evolution for $h_{1\text{-}2}/r = 40/3$ and $d/r = 25/9$. These values correspond to the transition between regimes (i) and (ii) of figure 10 according to (19).

We now turn to an estimate of the radius of the detached cavity. The data measured from the video images are plotted as a function of h/r in figure 15, with the size of the circles proportional to Fr as before. To estimate the cavity volume for regime (ii), we simply subtract the volume of the remaining jet 'tail', $\pi r^2(h-\frac{1}{2}Ut_c)$, from $\pi R_C^2(H_C-D)$ to find

$$\frac{V}{\gamma\pi r^3} = \left(2\frac{R_C^2}{r^2}+3\right)\left(\frac{\beta}{4}\frac{R_C}{r}\right)^{2/3} Fr^{1/3} - \frac{h}{r}, \tag{20}$$

where γ is a shape factor of order 1. With the previous values of the constants this relation becomes

$$V/\gamma\pi r^3 = 11Fr^{1/3} - h/r. \tag{21}$$

The corresponding radius R_B of the entrapped bubble is

$$R_B/r = [\tfrac{3}{4}\gamma(11Fr^{1/3} - h/r)]^{1/3}. \tag{22}$$

For a given Fr, the minimum of this quantity occurs when the portion of the jet that

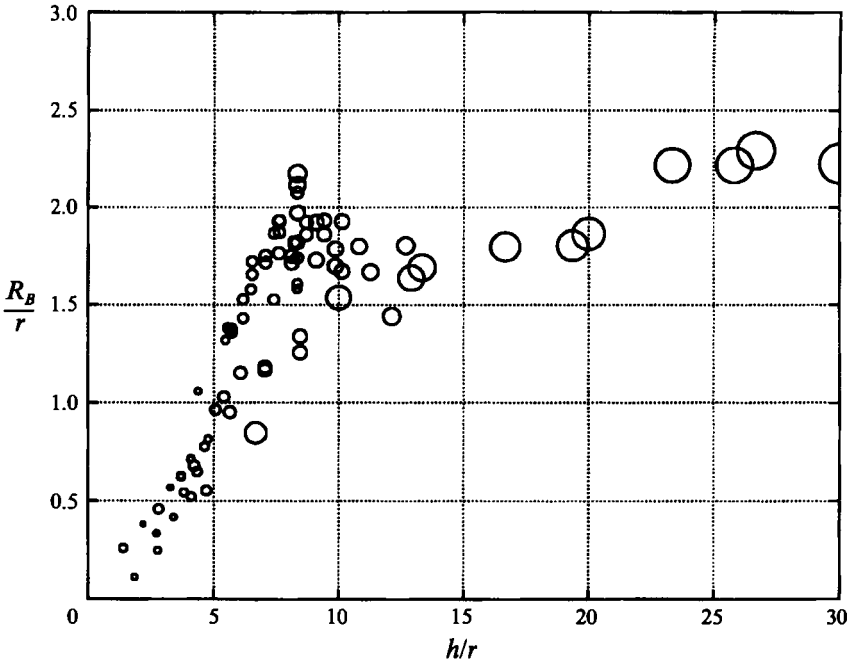

FIGURE 15. Equivalent spherical radius of the entrapped bubble measured from the high-speed video sequences. Scaled as for figure 9, the smallest circles are for $Fr = 5.46$ and the largest ones for $Fr = 50$.

has not yet penetrated the crater bottom reaches all the way up to the pinch-off point, i.e. for $h = h_{1\text{-}2}$ defined in (18). This minimum value is

$$R_B/r = (\tfrac{9}{2}\gamma)^{1/3} Fr^{1/9} \tag{23}$$

and the corresponding volume is

$$V/\gamma\pi r^3 = 6Fr^{1/3}. \tag{24}$$

Since in regime (i) the size of the entrapped cavity is independent of h, these results also represent the radius and the volume of the cavities entrapped when $h \geqslant h_{1\text{-}2}$. Conversely, for $h = h_{2\text{-}3}$, we have the maximum radius and volume for a given Froude number:

$$R_B/r = (6\gamma)^{1/3} Fr^{1/9} \tag{25}$$

and the corresponding volume

$$V/\gamma\pi r^3 = 8Fr^{1/3}. \tag{26}$$

The measured values of R_B shown in figure 15 falling in the parameter range where regimes (i) or (ii) are expected to prevail are shown in figure 16 after division by the expression on the right-hand side of (22) or (23), as appropriate, with $\gamma = \frac{1}{2}$. An acceptable agreement is found.

The previous estimates of cavity depth and bubble volume are not applicable to regime (iii) because here the lower part of the cavity starts collapsing inward before pinch-off. In this respect the situation here is reminiscent of the small-drop impact studied earlier. As in that case, it is possible to estimate the maximum cavity depth by assuming that the initial potential energy is converted to the potential energy of a

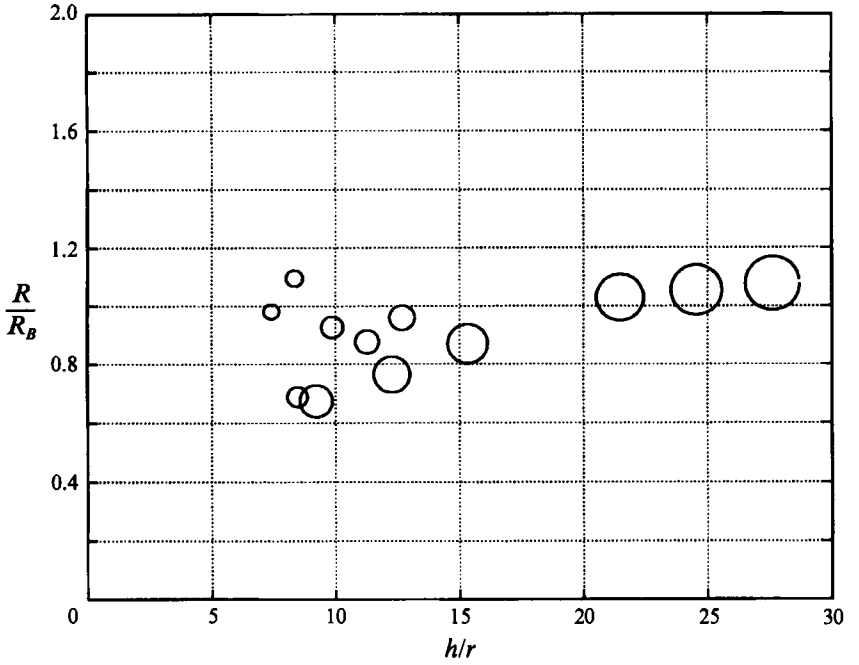

FIGURE 16. Measured equivalent spherical radii of the entrapped bubbles (from figure 15) divided by the predictions (22) or (23), as appropriate for cases falling in regimes (i) or (ii) of figure 10. The smallest circles are for $Fr = 6.85$ and the largest ones for $Fr = 45.9$.

cylindrical crater of radius R_C and depth H_P (Oğuz & Prosperetti 1990). In this way we find

$$H_P = \frac{r}{R_C} h \left(1 + \frac{2d}{h}\right)^{1/2}. \tag{27}$$

This estimate is expected to be applicable for $0 \leqslant h \leqslant h_{2\text{-}3}$. The observed values of cavity depth divided by H_P (with $R_C/r = 2$) are shown in figure 17. Clearly the scaling holds for sufficiently short jets.

The ratio of the two estimates (15) and (27) is

$$\frac{H_C}{H_P} = 3 \frac{R_C}{r} \left(\frac{h}{r}\right)^{-1/2} Fr^{-1/6}. \tag{28}$$

This fraction is smaller than 1 for the majority of the cases investigated here. This implies that, when the estimate (15) is applicable, only a fraction of the initial potential energy is stored in the crater. Aside from relatively small dissipative processes, the balance will be found in the residual kinetic energy of the liquid at the moment at which the cavity closes, and this energy is responsible for the secondary jet phenomenon shown e.g. in the last frame of figure 3.

In conclusion it is of some interest to contrast the present situation with the impact of a liquid drop on a plane liquid surface (Oğuz & Prosperetti 1990; Prosperetti & Oğuz 1993). In that case a bubble is only entrapped in a narrow range of the Weber–Froude number parameter space. In particular, for entrainment, the drop's Weber number must satisfy a bound of the form $We < Fr^{1/4}$, which is violated substantially in the cases considered here. This apparent inconsistency may be explained as follows. As far as the receiving liquid is concerned, the falling splash is a source of both mass and

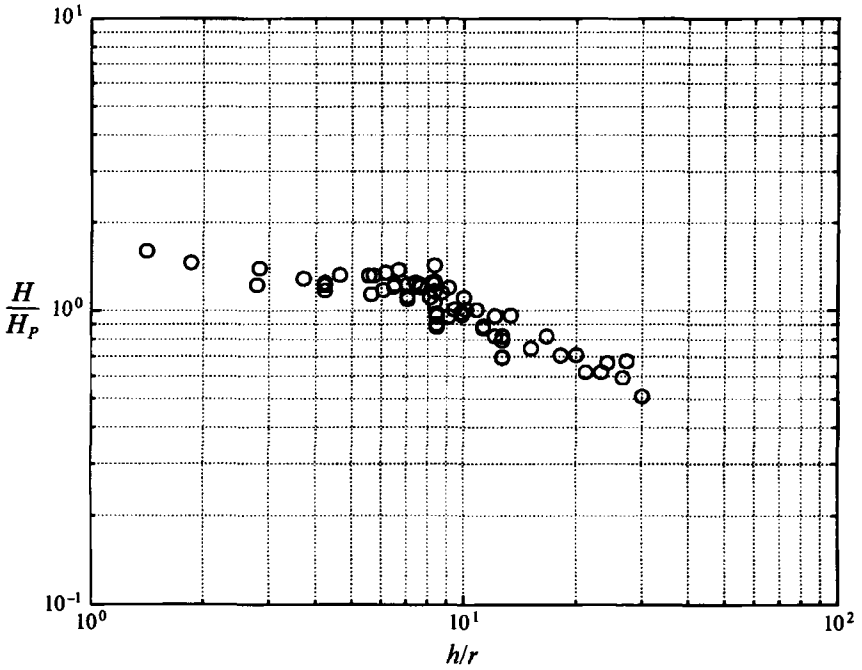

FIGURE 17. Measured cavity depths divided by H_P, (27), for the cases falling in regime (iii) of figure 10. The Froude number ranges between 7.41 and 50.

momentum. The mass source is omni-directional, and tends to produce a roughly hemispherical crater. The momentum source, on the other hand, is directed downward and gives rise to a roughly cylindrical cavity. Our experience with numerical calculations (some reported below, others in our earlier papers, and others unpublished) is that air is entrained only when the momentum-source aspect prevails. In the case of a drop, this is ensured by surface tension, which prevents an excessive spreading (or splattering) of the drop liquid. This effect becomes weaker in the case of larger drops, and this is the origin of the upper bound mentioned before. In the case considered here, the momentum-source aspect prevails due to the elongated shape of the impacting water mass in the direction of motion. This interpretation is substantiated by the fact that, experimentally, air is entrained only for jets with a sufficiently high aspect ratio.

5. Mathematical model

To proceed further with the analysis of the process at hand we need to resort to numerical simulation. We assume that at the initial instant the lower face of the falling water mass strikes the quiescent surface of the receiving liquid with the free-fall velocity $(2gd)^{1/2}$. We thus neglect waves over the surface of the jet and other complicating factors as a first approximation. Furthermore, in view of the magnitude of the impact energy, we also neglect the complex small-scale phenomena occurring when contact is established between the impacting mass and the host fluid. For example, a large number of small bubbles are entrained as a result of multiple-point contacts between the fluids and surface tension processes such as those described in Oğuz & Prosperetti (1989).

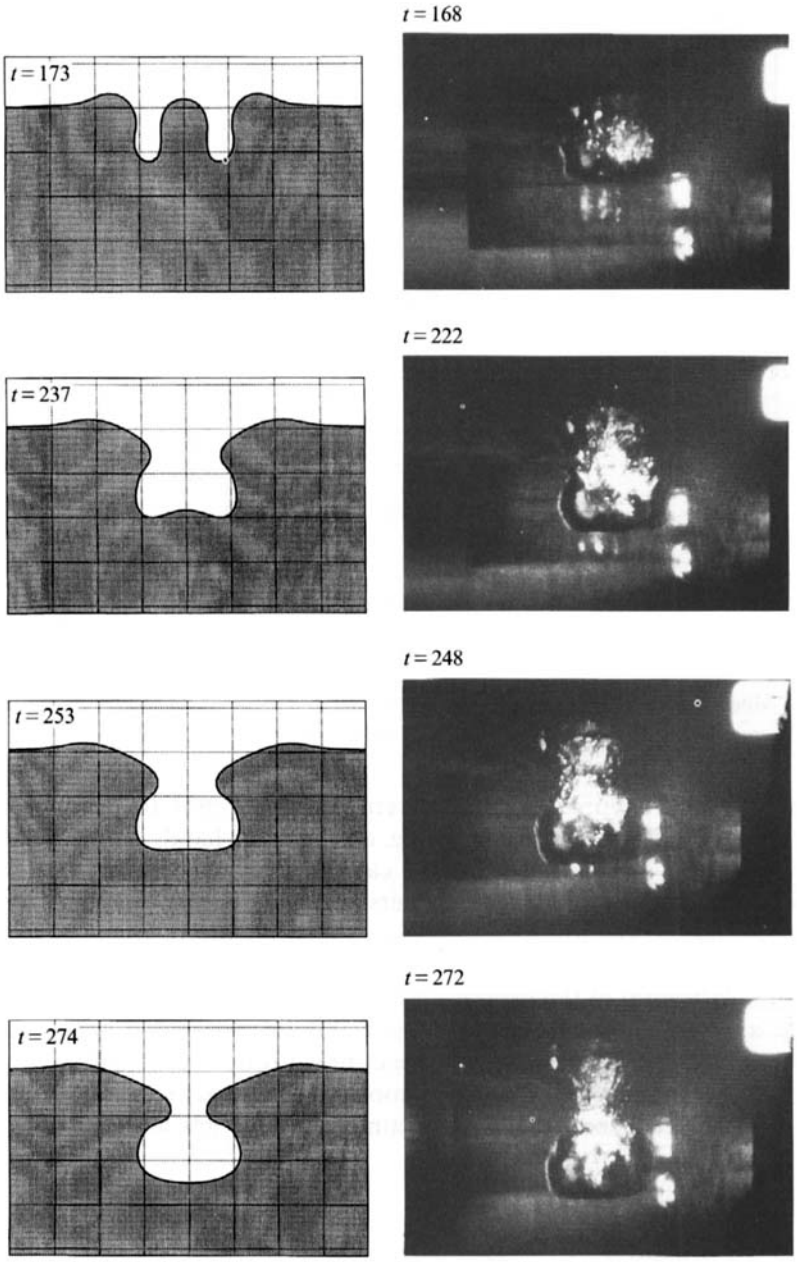

FIGURE 18. For caption see facing page.

Since initially the column of water is assumed to be in rigid-body motion and the tank water to be quiescent, there is no vorticity present in the system just before contact. If we neglect the curvature of the lower surface of the falling water, there is no discontinuity in tangential velocity across the interface at the time of contact and therefore no vorticity is generated there by the contact itself. On the assumption that the effect of viscosity is small, we therefore approximate the flow by an incompressible potential flow for which the velocity field is given by

$$\boldsymbol{u} = \nabla\phi \quad \text{with} \quad \nabla^2\phi = 0. \tag{29}$$

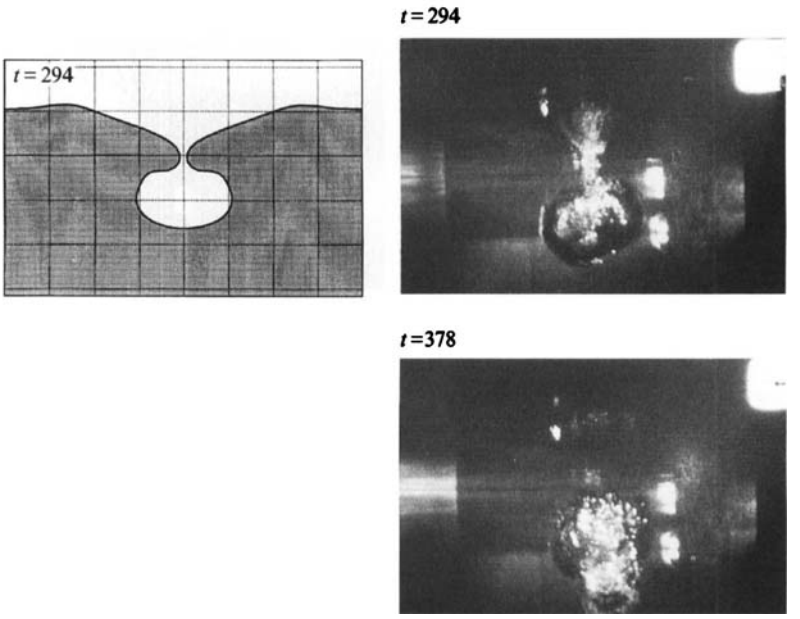

FIGURE 18. Comparison between measured (left) and computed (right) cavity shapes for the experimental conditions of figure 2, $Fr = 13.89$, $h/r = 8.33$, $d/r = 2.78$, $r = 54$ mm. This case falls in regime (ii) of figure 10.

At the free surface, the pressure is zero. By the use of the Bernoulli integral we then obtain

$$\frac{\mathrm{d}\phi}{\mathrm{d}t} = \tfrac{1}{2}|\nabla\phi|^2 + \frac{1}{Fr}z, \tag{30}$$

where $\mathrm{d}/\mathrm{d}t$ denotes the material derivative and the Froude number Fr is defined by (2). Here and in the following we use quantities made dimensionless with the characteristic length r and the characteristic velocity U defined by (1).

We assume axial symmetry, which greatly simplifies the numerical solution. The pool liquid is infinite and initially occupies the region $z \leqslant 0$. To avoid regions of sharp curvature, initially the top of the falling liquid mass is rounded to a hemisphere with radius r as shown in the first frame of figure 14. The height h is adjusted so that the mass of water above the free surface equals the water mass in the experiment. At $t = 0$ the surface $z = 0$ of the tank water, being at rest, is assigned zero potential. The velocity potential at the surface of the falling liquid is set to $-z/(1+h/2d)^{1/2}$. This corresponds to free fall over a distance equal to d. It may be noted that, with these initial conditions, the potential is continuous at the interface $z = 0$ at the moment of contact.

The boundary-integral technique is a particularly suitable for a potential-flow free-surface problem of this type. A number of different boundary-integral formulations exist in the literature (e.g. see Blake, Taib & Doherty 1986, 1987; Dommermuth & Yue 1987; Oğuz & Prosperetti 1989; Kucera & Best 1992; Best 1993). Here we have used the one developed in our previous study on the impact of a liquid drop (Oğuz & Prosperetti 1990) to which the reader is referred for details.

We have explored the sensitivity of the results to the precise shape of the impacting liquid by replacing the lower part of the cylinder by a truncated cone of different lengths and apertures. These shape variations were found to only affect the initial

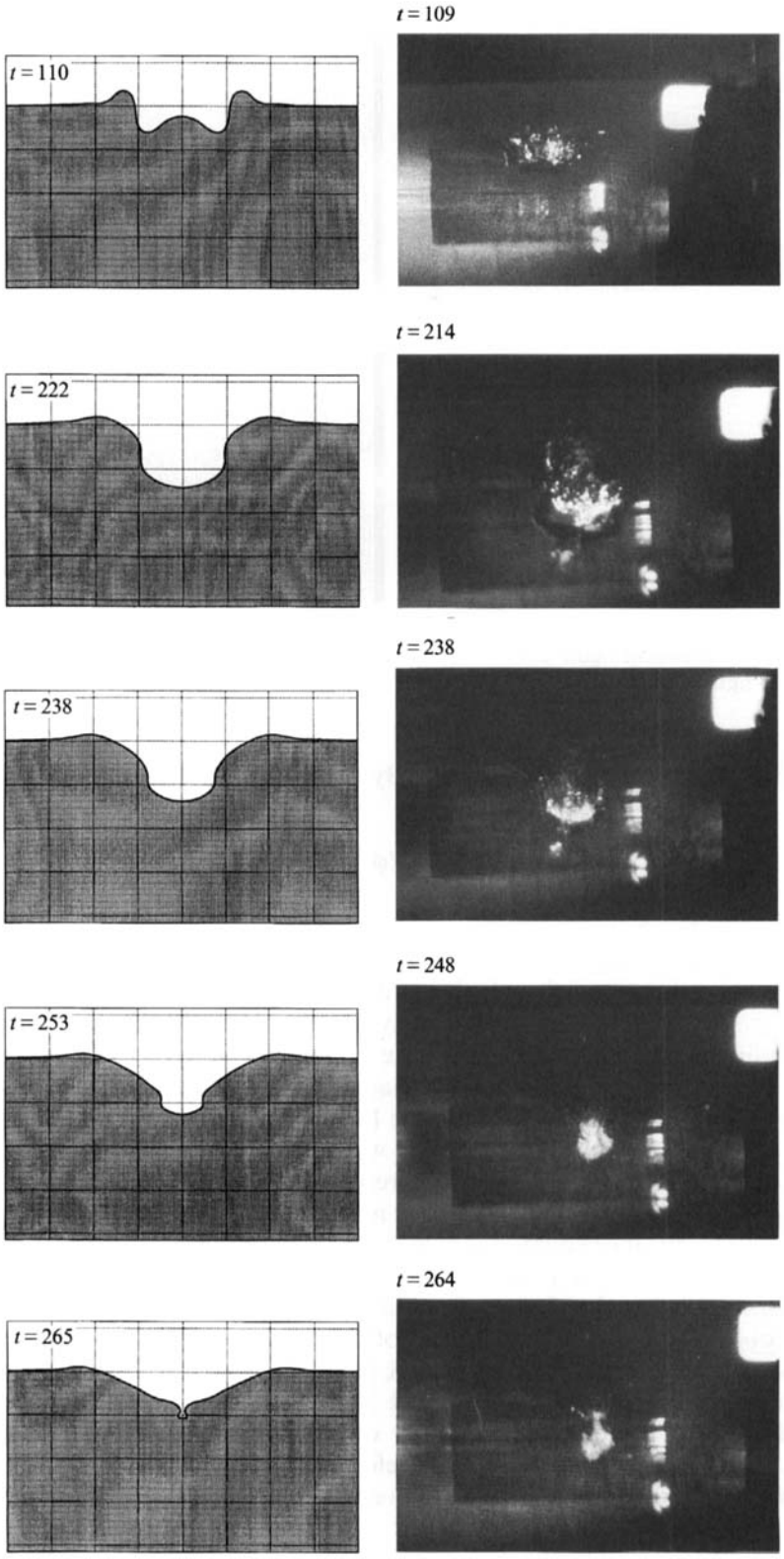

FIGURE 19. For caption see facing page.

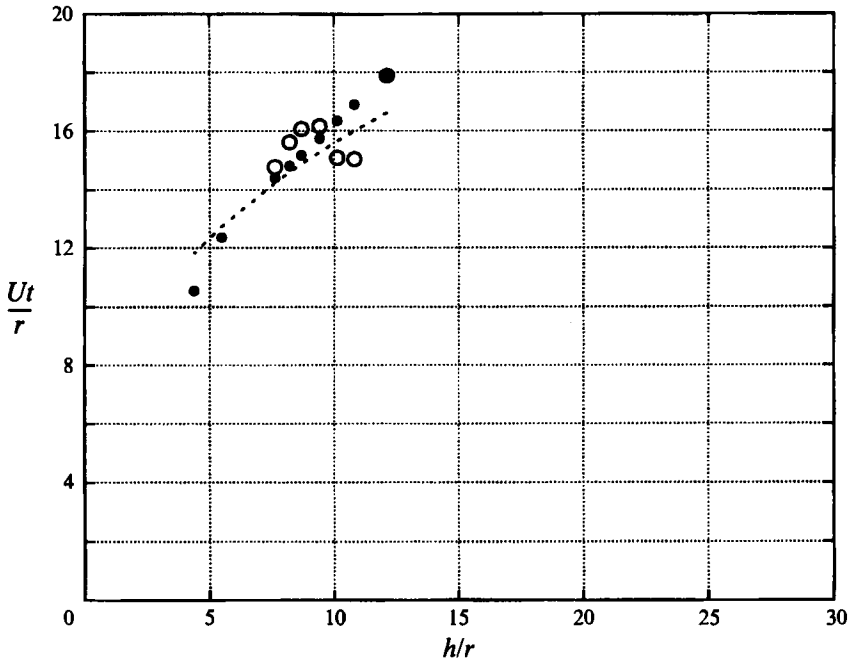

FIGURE 20. Numerical (solid circles) and experimental (open circles) cavity pinch-off times for different container radii and fixed liquid level, $h = 0.4$ m, and suspension height, $d = 0.15$ m. The dashed line is the estimate (14).

stages of the process, with a somewhat narrower cavity than that produced by the cylindrical shape. However, the subsequent development of the crater remained largely unchanged. This insensitivity to the initial shape had also been found in our earlier drop impact simulations (Oğuz & Prosperetti 1993).

6. Numerical simulations

Provided the Froude number is high enough, the cavity shapes predicted by the numerical simulations are all very similar. We present a comparison with the experimental ones for the case shown in figure 3 in figure 18. (Here the photos have been taken in the course of a run different from that of figure 3 but for the same experimental conditions.) The dimensionless numbers have the values $Fr = 13.9$, $We = 5670$, $R = 2.18 \times 10^4$. While in the general evolution of the free surface the numerical simulation resembles the video images, it differs from them in significant details. In the first place, the numerical cavity is not as deep as the experimental one. Secondly, the jet seems to be 'consumed' earlier in the calculation than in the experiment as revealed from the fact that, after the bottom of the numerical cavity has become convex, the experimental one is still flat as if the jet were still above it (recall that these are edge-on views and one cannot see inside the cavity due to refraction). Thirdly, at the moment of pinch-off, the aperture of the conical crater above the cavity is smaller in the experiment than in the calculation. These discrepancies, which are most likely all

FIGURE 19. Comparison between measured (left) and computed (right) cavity shapes for $Fr = 9.25$, $h/r = 3.70$, $d/r = 2.78$, $r = 54$ mm. This case falls in regime (iii) of figure 10.

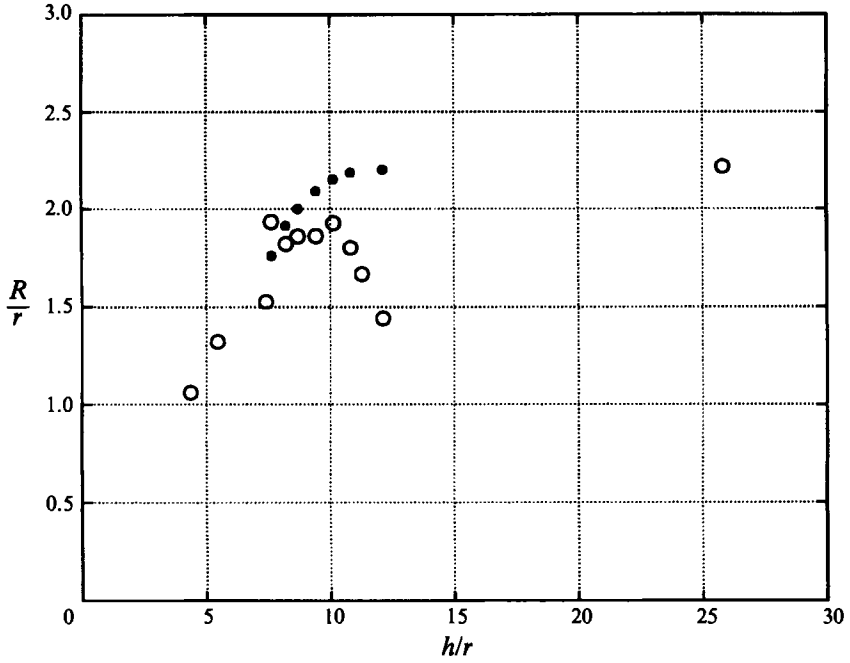

FIGURE 21. Comparison for the radii of the entrained bubble for the cases shown in figure 20.

related to the insufficient depth reached by the numerical cavity, were found to a smaller or greater degree in all the comparisons between experiment and numerical simulations that we have carried out. Another example is given in figure 7 where the cavity penetration *vs.* time is shown.

A possible explanation is the following. It is well known that in the *steady* flow of a jet impinging on a free surface, the streamlines also maintain a substantially downward direction below the surface of the host liquid (see e.g. Oğuz *et al.* 1992, figure 4). In other words, the incoming stream separates at the free surface, a fact that necessarily depends on the action of viscosity in the immediate neighbourhood of the point of entry. A similar process has been studied by Longuet-Higgins (1992, 1994) for the case of nonlinear capillary waves. The flow given by an inviscid irrotational model instead forces the fluid to spread radially along the free surface. In the case of present concern of the *transient* impact of a jet, one expects a short initial phase, in the course of which the irrotational-type flow prevails, which soon makes way for the separated flow regime. (As a proof of the initial potential-like flow one may cite the well-known fact that a drop of coloured liquid is reconstituted at the tip of the jet that issues from the bottom of the cavity that it produces, see Prosperetti and Oğuz 1993.) This might happen because, first, as the crater becomes deeper, the angle to be turned by the potential streamlines becomes larger and larger and, secondly, because surface-generated vorticity is continually injected in the flow. After the flow separates, the shear stress between the entering liquid and the free surface in its neighbourhood may be sufficient to push the latter downward. This process might also be aided by the roll-up into vortices of the vortex sheet forming at the separation point, that also would have the right circulation to promote a downward motion of the liquid.

These considerations might explain the greater depth reached by the cavity in the experiment. In truth, an observation against this scenario is the lack of small bubbles

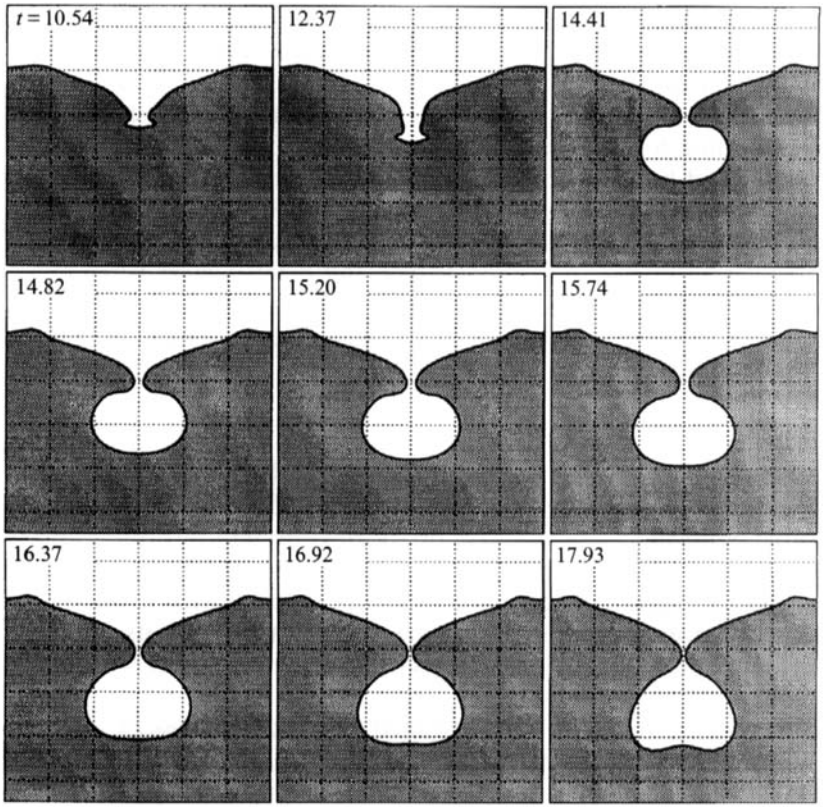

FIGURE 22. Last computed free-surface configuration, just before the pinch-off of the cavity, for the theoretical points of figures 20 and 21. Here $h/d = 8/3$ and $h/r = 12.12, 10.81, 10.12, 9.41, 8.70, 8.21, 7.62, 5.46$ and 4.37. The times indicated are in units of r/U.

below the main cavity that one would expect to be entrained at the separation line. Unfortunately we are unable to clarify this point further at this time.

It was mentioned earlier that the mechanics of the process is very different in the case of weak impacts. We show in figure 19 a comparison between experiment and calculation for the same case as the previous figure except that the water level is $h = 0.20$ m rather than 0.45, so that $h/r = 3.7$. For this case, the value h_{2-3} marking the boundary between regimes (ii) and (iii) of figure 10 is 0.34 m, so that we are clearly in case (iii). The numerical simulation predicts the entrapment of a very small bubble. Experimentally, one sees a cloud of small bubbles with possibly a somewhat bigger cavity in the centre. Again, while the correspondence between experiment and theory is not perfect, the calculation does indicate a very different behaviour from the previous case.

In order to illustrate further aspects of the numerical prediction, we compare in figure 20 experimental (open circles) and numerical cavity pinch-off times for different radii and fixed liquid depth in the container, $h = 0.4$ m, and suspension height, $d = 0.15$ m. The dashed line is the expression (14). The theoretical predictions are quite close to the data. In particular, it may be noted that the last experimental and numerical points fall on top of each other. Comparisons for the radii of the entrained bubble for the same cases are shown in figure 21. Although there is agreement in some cases, there also are substantial differences at the smaller r (since h is fixed here, increasing h/r implies decreasing r). From figure 15 it is seen that, in the range where

the greatest discrepancies exist, there is a rather large scatter in the experimental data. The implication seems to be that r cannot be quite scaled out as we have done. We are unclear as to the cause of this phenomenon.

Finally, in figure 22, we show the last computed free-surface configuration for the cases corresponding to the points shown in figures 20 and 21. Here h and d are fixed with $h/d = 8/3$ and h/r between 4.37 and 12.12. In the case of the two smallest values the pinch-off time is very close to the filling time of the cavity and the entrapped bubble does not fully form. Experimentally, this is probably the situation where a cloud of small bubbles is entrained. As h/r increases, full cavities start being entrapped. For larger h/r the bottom of the cavity becomes less and less rounded as the transition between regimes (iii) and (ii) is approached. The last case is one of incipient regime (ii).

7. Conclusion

We have studied the normal impact of a cylindrical liquid mass on a liquid surface. We have found that a large bubble is entrained for sufficiently large energies and aspect ratios. Simple physical arguments have provided considerable insight into the process, with better than order-of-magnitude agreement with observation. In particular, we have been able to estimate the width and depth of the cavity formed in the water, the volume of the entrapped bubble, and the time required for its pinch-off. Inviscid irrotational numerical simulations are also in broad agreement with the experiment, although some differences remain.

A key point on which this work fails to shed light is the process by which the particles of the falling liquid penetrate under the surface. The separation phenomenon responsible for this effect appears to be crucial for a number of air-entraining flows but still remains little understood.

This study has been supported by the Ocean Acoustics and Fluid Dynamics Programs of the Office of Naval Research.

REFERENCES

BEST, J. P. 1993 The formation of toroidal bubbles upon the collapse of transient cavities. *J. Fluid Mech.* **251**, 79–107.

BIRKHOFF, G. & ZARANTONELLO, E. H. 1957 *Jets, Wakes and Cavities.* Academic.

BLAKE, J. R., TAIB, B. B. & DOHERTY, G. 1986 Transient cavities near boundaries. Part 1. Rigid boundary. *J. Fluid Mech.* **170**, 479–497.

BLAKE, J. R., TAIB, B. B. & DOHERTY, G. 1987 Transient cavities near boundaries. Part 2. Free surface. *J. Fluid Mech.* **181**, 197–212.

CHAHINE, G. L., WENK, K., GUPTA, S. & ELMORE, P. A. 1991 Bubble formation following drop impact at a free surface. In *Cavitation and Multiphase Forum* (ed. O. Furuya & H. Kato), vol. 109, pp. 63–68. ASME.

DING, L. & FARMER, D. M. 1994 On the dipole acoustic source level of breaking waves. *J. Acoust. Soc. Am.* **96**, 3036–3044.

DOMMERMUTH, D. G. & YUE, D. K. P. 1987 Numerical simulations of nonlinear axisymmetric flows with a free surface. *J. Fluid Mech.* **178**, 195–219.

FARMER, D. M. & DING, L. 1992 Coherent acoustical radiation from breaking waves. *J. Acoust. Soc. Am.* **92**, 397–402.

FRANZ, G. J. 1959 Splashes as sources of sound in liquids. *J. Acoust. Soc. Am.* **31**, 1080–1096.

HOLLETT, R. D. 1994 Observations of underwater sound at frequencies below 1500 Hz from breaking waves at sea. *J. Acoust. Soc. Am.* **95**, 165–170.

KOLAINI, A. R. & CRUM, L. A. 1994 Observations of underwater sound from laboratory breaking waves and the implications concerning ambient noise in the ocean. *J. Acoust. Soc. Am.* **96**, 1755–1765.

KOLAINI, A. R., ROY, R. A., CRUM, L. A. & MAO, Y. 1993 Low-frequency underwater sound generation by impacting transient water jets. *J. Acoust. Soc. Am.* **94**, 2809–2820.

KUCERA, A. & BEST, J. P. 1992 A numerical investigation of non-spherical rebounding bubbles. *J. Fluid Mech.* **245**, 137–154.

LAMARRE, E. & MELVILLE, W. K. 1994 Void-fraction measurements and sound-speed fields in bubble plumes generated by breaking waves. *J. Acoust. Soc. Am.* **95**, 1317–1328.

LOEWEN, M. R. & MELVILLE, W. K. 1994 An experimental investigation of the collective oscillations of bubble plumes entrained by breaking waves. *J. Acoust. Soc. Am.* **95**, 1329–1343.

LONGUET-HIGGINS, M. S. 1989 Report of ONR Planning Group on Acoustic Sea Surface Scattering. *MIT Tech. Rep.*, 7–10 March 1989.

LONGUET-HIGGINS, M. S. 1990 An analytic model of sound production by rain-drops. *J. Fluid Mech.* **214**, 395–410.

LONGUET-HIGGINS, M. S. 1992 Capillary rollers and bores. *J. Fluid Mech.* **240**, 659–679.

LONGUET-HIGGINS, M. S. 1994 Shear instability in spilling breakers. *Proc. R. Soc. Lond.* A **446**, 399–409.

MEDWIN, H. & BEAKY, M. M. 1989 Bubble sources of the Knudsen sea noise spectra. *J. Acoust. Soc. Am* **86**, 1124–1130.

MEDWIN, H. & DANIEL, A. C. 1990 Acoustical measurements of bubble production by spilling breakers. *J. Acoust. Soc. Am.* **88**, 408–412.

MINNAERT, M. 1933 On musical air bubbles and the sounds of running water. *Phil. Mag.* **16**, 235–248.

OĞUZ, H. N., LEZZI, A. M. & PROSPERETTI, A. 1992 Examples of air-entraining flows. *Phys. Fluids* **4**, 649–651.

OĞUZ, H. N. & PROSPERETTI, A. 1989 Surface-tension effects in the contact of liquid surfaces. *J. Fluid Mech.* **203**, 149–171.

OĞUZ, H. N. & PROSPERETTI, A. 1990 Bubble entrainment by the impact of drops on liquid surfaces. *J. Fluid Mech.* **219**, 143–179.

OĞUZ, H. N. & PROSPERETTI, A. 1991 Numerical calculation of the underwater noise of rain. *J. Fluid Mech.* **228**, 417–442.

OĞUZ, H. N. & PROSPERETTI, A. 1993 Drop impact and the underwater noise of rain. In *Natural Physical Sources of Underwater Sound* (ed. B. R. Kerman), pp. 669–682. Reidel.

PROSPERETTI, A 1988 Bubble related ambient noise in the ocean. *J. Acoust. Soc. Am.* **84**, 1042–1054.

PROSPERETTI, A. & OĞUZ, H. N. 1993 The impact of drops on liquid surfaces and the underwater noise of rain. *Ann. Rev. Fluid Mech.* **25**, 577–602.

PUMPHREY, H. C. & CRUM, L. A. 1988 Acoustic emissions associated with drop impacts. In *Sea Surface Sound* (ed. B. R. Kerman), pp. 463–483. Kluwer.

PUMPHREY, H. C. & CRUM, L. A. 1990 Free oscillations of near-surface bubbles as a source of the underwater noise of rain. *J. Acoust. Soc. Am.* **87**, 142–148.

PUMPHREY, H. C., CRUM, L. A. & BJØRNØ, L. 1989 Underwater sound produced by individual drop impacts and rainfall. *J. Acoust. Soc. Am.* **85**, 1518–1526.

PUMPHREY, H. C. & ELMORE, P. A. 1990 The entrainment of bubbles by drop impacts. *J. Fluid Mech.* **220**, 539–567.

STROUD, J. S. & MARSTON, P. L. 1993 Optical detection of transient bubble oscillations associated with the underwater noise of rain. *J. Acoust. Soc. Am.* **94**, 2788–2792.